

March 2010

Effects of Residue Background Events in Direct Dark Matter Detection Experiments on the Determination of the WIMP Mass

YU-TING CHOU¹ and CHUNG-LIN SHAN^{2,3}

¹ *Institute of Physics, National Chiao Tung University
No. 1001, University Road, Hsinchu City 30010, Taiwan, R.O.C.
E-mail: yuting.py97g@nctu.edu.tw*

² *Department of Physics, National Cheng Kung University
No. 1, University Road, Tainan City 70101, Taiwan, R.O.C.
E-mail: clshan@mail.ncku.edu.tw*

³ *Physics Division, National Center for Theoretical Sciences
No. 101, Sec. 2, Kuang-Fu Road, Hsinchu City 30013, Taiwan, R.O.C.*

Abstract

In the earlier work on the development of a model-independent data analysis method for determining the mass of Weakly Interacting Massive Particles (WIMPs) by using measured recoil energies from direct Dark Matter detection experiments directly, it was assumed that the analyzed data sets are background-free, i.e., all events are WIMP signals. In this article, as a more realistic study, we take into account a fraction of possible residue background events, which pass all discrimination criteria and then mix with other real WIMP-induced events in our data sets. Our simulations show that, for the determination of the WIMP mass, the maximal acceptable fraction of residue background events in the analyzed data sets of $\mathcal{O}(50)$ total events is $\sim 20\%$, for background windows of the entire experimental possible energy ranges, or in low energy ranges; while, for background windows in relatively higher energy ranges, this maximal acceptable fraction of residue background events can not be larger than $\sim 10\%$. For a WIMP mass of 100 GeV with 20% background events in the windows of the entire experimental possible energy ranges, the reconstructed WIMP mass and the 1σ statistical uncertainty are $\sim 97 \text{ GeV}^{+61\%}_{-35\%}$ ($\sim 94 \text{ GeV}^{+55\%}_{-33\%}$ for background-free data sets).

1 Introduction

Currently, direct Dark Matter detection experiments searching for Weakly Interacting Massive Particles (WIMPs) are one of the promising methods for understanding the nature of Dark Matter and identifying them among new particles produced at colliders as well as reconstructing the (sub)structure of our Galactic halo [1, 2, 3, 4]. In order to determine the mass of halo WIMPs *without* making any assumptions about their density near the Earth or their velocity distribution *nor* knowing their scattering cross section on nucleus, a model-independent method by combining two experimental data sets with two different target nuclei has been developed [5, 6]. This method builds on the earlier work on the reconstruction of the (moments of the) one-dimensional velocity distribution function of halo WIMPs, $f_1(v)$, by using data from direct detection experiments [7].

In the analysis of reconstructing $f_1(v)$, the moments of the WIMP velocity distribution function can be determined from experimental data directly with an *unique* input information about the WIMP mass m_χ . Hence, one can simply require that the values of a given moment of $f_1(v)$ determined by two experiments agree¹. This leads to a simple analytic expression for determining m_χ [5, 6], where each moment can in principle be used. Additionally, under the assumptions that the spin-independent (SI) WIMP-nucleus interaction dominates over the spin-dependent (SD) one and the SI WIMP coupling on protons is approximately the same as that on neutrons, a second analytic expression for determining m_χ has been derived [6]. Finally, by combining the first estimators for different moments with each other and with the second estimator, one can yield the best-fit WIMP mass as well as minimize its statistical uncertainty.

In the work on the development of the model-independent data analysis procedure for the determination of the WIMP mass, it was assumed that the analyzed data sets are background-free, i.e., all events are WIMP signals. Active background discrimination techniques should make this condition possible. For example, the ratio of the ionization to recoil energy, the so-called “ionization yield”, used in the CDMS-II experiment provides an event-by-event rejection of electron recoil events to be better than 10^{-4} misidentification [8]. By combining the “phonon pulse timing parameter”, the rejection ability of the misidentified electron recoils (most of them are “surface events” with sufficiently reduced ionization energies) can be improved to be $< 10^{-6}$ for electron recoils [8]. Moreover, as demonstrated by the CRESST collaboration [9], by means of inserting a scintillating foil, which causes some additional scintillation light for events induced by α -decay of ^{210}Po and thus shifts the pulse shapes of these events faster than pulses induced by WIMP interactions in the crystal, the pulse shape discrimination (PSD) technique can then easily distinguish WIMP-induced nuclear recoils from those induced by backgrounds².

However, as the most important issue in all underground experiments, the signal identification ability and possible residue background events which pass all discrimination criteria and then mix with other real WIMP-induced events in our data sets should also be considered. Therefore, in this article, as a more realistic study, we take into account different fractions of residue background events mixed in experimental data sets and want to study how well the model-independent method could reconstruct the input WIMP mass by using these “impure” data sets and how “dirty” these data sets could be to be still useful.

The remainder of this article is organized as follows. In Sec. 2 we review the recoil spectrum of elastic WIMP-nucleus scattering and introduce two kinds of background spectrum used in

¹Note that, as demonstrated and discussed in Ref. [6], this condition requires an algorithmic procedure for matching the maximal cut-off energies of the analyzed data sets.

²For more details about background discrimination techniques and status in currently running and projected direct detection experiments, see e.g., Refs. [10, 11, 12]

our simulations. In Sec. 3 we first review briefly the model-independent method for the determination of the WIMP mass. Then we show numerical results of the reconstructed WIMP mass by using mixed data sets with different fractions of residue background events based on Monte Carlo simulations. We conclude in Sec. 4. Some technical details will be given in an appendix.

2 Signal and background spectra

In this section we first review the recoil spectrum of elastic WIMP–nucleus scattering. Then we introduce two forms of background spectrum which will be used in our simulations. Some numerical results of the measured energy spectrum superposed by the WIMP scattering and background spectra will also be discussed.

2.1 Elastic WIMP–nucleus scattering spectrum

The basic expression for the differential event rate for elastic WIMP–nucleus scattering is given by [3]:

$$\frac{dR}{dQ} = \mathcal{A} F^2(Q) \int_{v_{\min}}^{v_{\max}} \left[\frac{f_1(v)}{v} \right] dv. \quad (1)$$

Here R is the direct detection event rate, i.e., the number of events per unit time and unit mass of detector material, Q is the energy deposited in the detector, $F(Q)$ is the elastic nuclear form factor, $f_1(v)$ is the one-dimensional velocity distribution function of the WIMPs impinging on the detector, v is the absolute value of the WIMP velocity in the laboratory frame. The constant coefficient \mathcal{A} is defined as

$$\mathcal{A} \equiv \frac{\rho_0 \sigma_0}{2m_\chi m_{\text{r},\text{N}}^2}, \quad (2)$$

where ρ_0 is the WIMP density near the Earth and σ_0 is the total cross section ignoring the form factor suppression. The reduced mass $m_{\text{r},\text{N}}$ is defined by

$$m_{\text{r},\text{N}} \equiv \frac{m_\chi m_{\text{N}}}{m_\chi + m_{\text{N}}}, \quad (3)$$

where m_χ is the WIMP mass and m_{N} that of the target nucleus. Finally, v_{\min} is the minimal incoming velocity of incident WIMPs that can deposit the energy Q in the detector:

$$v_{\min} = \alpha \sqrt{Q} \quad (4)$$

with the transformation constant

$$\alpha \equiv \sqrt{\frac{m_{\text{N}}}{2m_{\text{r},\text{N}}^2}}, \quad (5)$$

and v_{\max} is the maximal WIMP velocity in the Earth's reference frame, which is related to the escape velocity from our Galaxy at the position of the Solar system, $v_{\text{esc}} \gtrsim 600$ km/s. Note that, as will be shown below, the Earth's velocity relative to the Galactic halo is time-dependent, and considering the random motion of WIMPs in the Galaxy, the relation between the one-dimensional cut-off v_{\max} and the three-dimensional one v_{esc} is thus rather complicated. Nevertheless, it is unlikely to affect the event rate as well as the results shown in this article significantly. In the literature, for simplicity and practical uses, v_{\max} is often set as ∞ (e.g., [13, 14, 15]).

2.1.1 One-dimensional WIMP velocity distribution function

The simplest semi-realistic model halo is a spherical isothermal Maxwellian halo. More realistically, one has to take into account the orbital motion of the Solar system around the Galaxy as well as that of the Earth around the Sun. The one-dimensional velocity distribution function of this shifted Maxwellian halo can be expressed as [2, 3, 7]

$$f_{1,\text{sh}}(v) = \frac{1}{\sqrt{\pi}} \left(\frac{v}{v_e v_0} \right) \left[e^{-(v-v_e)^2/v_0^2} - e^{-(v+v_e)^2/v_0^2} \right]. \quad (6)$$

Here $v_0 \simeq 220$ km/s is the orbital velocity of the Sun in the Galactic frame, and v_e is the Earth's velocity in the Galactic frame [16, 3, 4]:

$$v_e(t) = v_0 \left[1.05 + 0.07 \cos \left(\frac{2\pi(t - t_p)}{1 \text{ yr}} \right) \right]; \quad (7)$$

$t_p \simeq$ June 2nd is the date on which the velocity of the Earth relative to the WIMP halo is maximal. Substituting Eq. (6) into Eq. (1), an analytic form of the integral over the velocity distribution function can be given as [17]

$$\int_{v_{\min}}^{v_{\max}} \left[\frac{f_{1,\text{sh}}(v)}{v} \right] dv = \frac{1}{2v_e} \left\{ \left[\text{erf} \left(\frac{\alpha\sqrt{Q}+v_e}{v_0} \right) - \text{erf} \left(\frac{\alpha\sqrt{Q}-v_e}{v_0} \right) \right] - \left[\text{erf} \left(\frac{v_{\max}+v_e}{v_0} \right) - \text{erf} \left(\frac{v_{\max}-v_e}{v_0} \right) \right] \right\}. \quad (8)$$

Here $\text{erf}(x)$ is the error function, defined as

$$\text{erf}(x) = \frac{2}{\sqrt{\pi}} \int_0^x e^{-t^2} dt.$$

On the other hand, for practical, numerical uses, an approximate form of the integral over $f_1(v)$ was introduced as [2]

$$\int_{v_{\min}}^{\infty} \left[\frac{f_1(v)}{v} \right] dv = c_0 \left(\frac{2}{\sqrt{\pi} v_0} \right) e^{-\alpha^2 Q/c_1 v_0^2}, \quad (9)$$

where c_0 and c_1 are two fitting parameters of order unity. Not surprisingly, their values depend on the Galactic orbital and escape velocities, the target nucleus, the threshold energy of the experiment, as well as on the mass of incident WIMPs. Note that, the characteristic energy $Q_{\text{ch}} \equiv c_1 v_0^2 / \alpha^2$ and thus the shape of the recoil spectrum depend highly on the WIMP mass: for light WIMPs ($m_\chi \ll m_N$), $Q_{\text{ch}} \propto m_\chi^2$ and the recoil spectrum drops sharply with increasing recoil energy, while for heavy WIMPs ($m_\chi \gg m_N$), $Q_{\text{ch}} \sim \text{const.}$ and the spectrum becomes flatter.

2.1.2 Spin-independent WIMP–nucleus cross section

In most theoretical models, the spin-independent (SI) WIMP–nucleus interaction with an atomic mass number $A \gtrsim 30$ dominates over the spin-dependent (SD) one [3, 4]. Additionally, for the lightest supersymmetric neutralino which is perhaps the best motivated WIMP candidate [3, 4], and for all WIMPs which interact primarily through Higgs exchange, the SI scalar coupling is approximately the same on both protons p and neutrons n, the “pointlike” cross section σ_0 in Eq. (2) can thus be written as

$$\sigma_0 = A^2 \left(\frac{m_{\text{r},\text{N}}}{m_{\text{r},\text{p}}} \right)^2 \sigma_{\chi\text{p}}^{\text{SI}}, \quad (10)$$

where

$$\sigma_{\chi p}^{\text{SI}} = \left(\frac{4}{\pi}\right) m_{r,p}^2 |f_p|^2 \quad (11)$$

is the SI WIMP–proton cross section, f_p is the effective $\chi\chi pp$ four–point coupling, A is the atomic mass number of the target nucleus, and $m_{r,p}$ is the reduced mass of the WIMP mass m_χ and the proton mass m_p .

For the SI WIMP–nucleus cross section, an analytic form for the elastic nuclear form factor, inspired by the Woods–Saxon nuclear density profile, has been suggested by Engel as [18, 3, 4]³

$$F_{\text{WS}}^2(Q) = \left[\frac{3j_1(qR_1)}{qR_1} \right]^2 e^{-(qs)^2}. \quad (12)$$

Here $j_1(x)$ is a spherical Bessel function, $q = \sqrt{2m_N Q}$ is the transferred 3-momentum, given as a function of the recoil energy transferred from the incident WIMP to the target nucleus, Q , and the mass of the target nucleus, m_N ; $R_1 = \sqrt{R_A^2 - 5s^2}$ is the effective nuclear radius with $R_A \simeq 1.2 A^{1/3}$ fm and the nuclear skin thickness $s \simeq 1$ fm.

2.2 Background spectrum

For our simulations with residue background events, two forms of background spectrum are considered. The simplest choice for the background spectrum is the constant spectrum:

$$\left(\frac{dR}{dQ} \right)_{\text{bg, const}} = 1. \quad (13)$$

More realistically, inspired by Ref. [14], we introduce a *target–dependent exponential* spectrum given by

$$\left(\frac{dR}{dQ} \right)_{\text{bg, ex}} = \exp \left(-\frac{Q/\text{keV}}{A^{0.6}} \right). \quad (14)$$

Here Q is the recoil energy, A is the atomic mass number of the target nucleus. The power index of A , 0.6, is an empirical constant, which has been chosen so that the exponential background spectrum is somehow *similar to*, but still *different from* the expected recoil spectrum of the target nuclei; otherwise, there is in practice no difference between the WIMP scattering and background spectra. Note that, among different possible choices (e.g., the exponential form used in Ref. [14]), we use in our simulations the atomic mass number A as the simplest, unique characteristic parameter in the general analytic form (14) for defining the residue background spectrum for *different* target nuclei. However, it does *not* mean that the (superposition of the real) background spectra would depend simply/primarily on A or on the mass of the target nucleus, m_N . In other words, it is practically equivalent to use expression (14) or $(dR/dQ)_{\text{bg, ex}} = e^{-Q/13.5 \text{ keV}}$ directly for a ⁷⁶Ge target.

Note also that, firstly, two forms of background spectrum given in Eqs. (13) and (14) are rather naive; however, since we consider here *only a few residue* background events induced by perhaps *two or more* different sources, pass all discrimination criteria, and then mix with other WIMP–induced events in our data sets of $\mathcal{O}(50)$ *total* events, exact forms of different background spectra are actually not very important and these two spectra, in particular, the exponential one, should practically not be unrealistic⁴. Secondly, for using the maximum likelihood analysis

³Other commonly used analytic forms for the nuclear form factor for the SI WIMP–nucleus cross section can be found in Ref. [17].

⁴Other (more realistic) forms for background spectrum (perhaps also for some specified targets/experiments) can be tested on the AMIDAS website [19, 20].

to determine the WIMP mass, as described in Refs. [21, 14, 13], a prior knowledge about the WIMP scattering spectrum and eventually about the background spectrum is essential [14]. In contrast, as demonstrated in Ref. [6] and will be reviewed in the next section, the model-independent data analysis procedure requires only measured recoil energies (induced mostly by WIMPs and occasionally by background sources) from two experimental data sets with different target nuclei. Therefore, for applying this method to future real data from direct detection experiments, the prior knowledge about (different) background source(s) is *not required at all*.

2.3 Measured energy spectrum

In Figs. 1 we show measured energy spectra (solid red histograms) for a ^{76}Ge target with six different WIMP masses: 10, 25, 50, 100, 250, and 500 GeV based on Monte Carlo simulations. The dotted blue curves are the elastic WIMP-nucleus scattering spectra for the shifted Maxwellian velocity distribution given in Eq. (6) with $v_0 = 220$ km/s, $v_e = 1.05 v_0$,⁵ and $v_{\text{esc}} = 700$ km/s and the Woods-Saxon elastic nuclear form factor in Eq. (12). The dashed green curves are the exponential background spectra given in Eq. (14), which have been normalized so that the ratios of the areas under these background spectra to those under the (dotted blue) WIMP scattering spectra are equal to the background-signal ratio in the whole data sets (i.e., 20% backgrounds to 80% signals shown in Figs. 1). The experimental threshold energy has been assumed to be negligible and the maximal cut-off energy is set as 100 keV. 5,000 experiments with 500 total events on average in each experiment have been simulated.

The measured energy spectra (solid red histograms) shown in Figs. 1 are averaged over the simulated experiments. Five bins with linearly increased bin widths have been used for binning generated signal and background events. As argued in Ref. [7], for reconstructing the one-dimensional WIMP velocity distribution function, this unusual, particular binning has been chosen in order to accumulate more events in high energy ranges and thus to reduce the statistical uncertainties in high velocity ranges. However, as we will show later, for the determination of the WIMP mass, one needs either events in the *first* energy bin or *all* events in the whole data set. Hence, there is in practice no difference between using an equal bin width for all bins or the (linearly) increased bin widths.

Note here that, firstly, the possible energy ranges in which residue background events exist (the background windows) have been assumed to be the same as the entire experimental possible energy ranges (e.g., between 0 and 100 keV for simulations shown in Figs. 1). Secondly, the actual numbers of signal and background events in each simulated experiment are Poisson-distributed around their expectation values *independently*. This means that, for example, for simulations shown in Figs. 1 we generate 400 (100) events on average for WIMP signals (backgrounds) and the total event number recorded in one experiment is then the sum of these two numbers. Thirdly, for the simulations demonstrated here as well as in the next section, we assumed that all experimental systematic uncertainties as well as the uncertainty on the measurement of the recoil energy could be ignored. The energy resolution of most existing detectors is so good that its error can be neglected compared to the statistical uncertainty for the foreseeable future with pretty few events.

In Figs. 1 it can be found that, as mentioned earlier, the shape of the WIMP scattering spectrum depends highly on the WIMP mass: for light WIMPs ($m_\chi \lesssim 50$ GeV), the recoil spectra drop sharply with increasing recoil energies, while for heavy WIMPs ($m_\chi \gtrsim 100$ GeV), the spectra become flatter. In contrast, the exponential background spectra shown here depend only on the

⁵The time dependence of the Earth's velocity in the Galactic frame, the second term of $v_e(t)$ in Eq. (7), has been ignored.

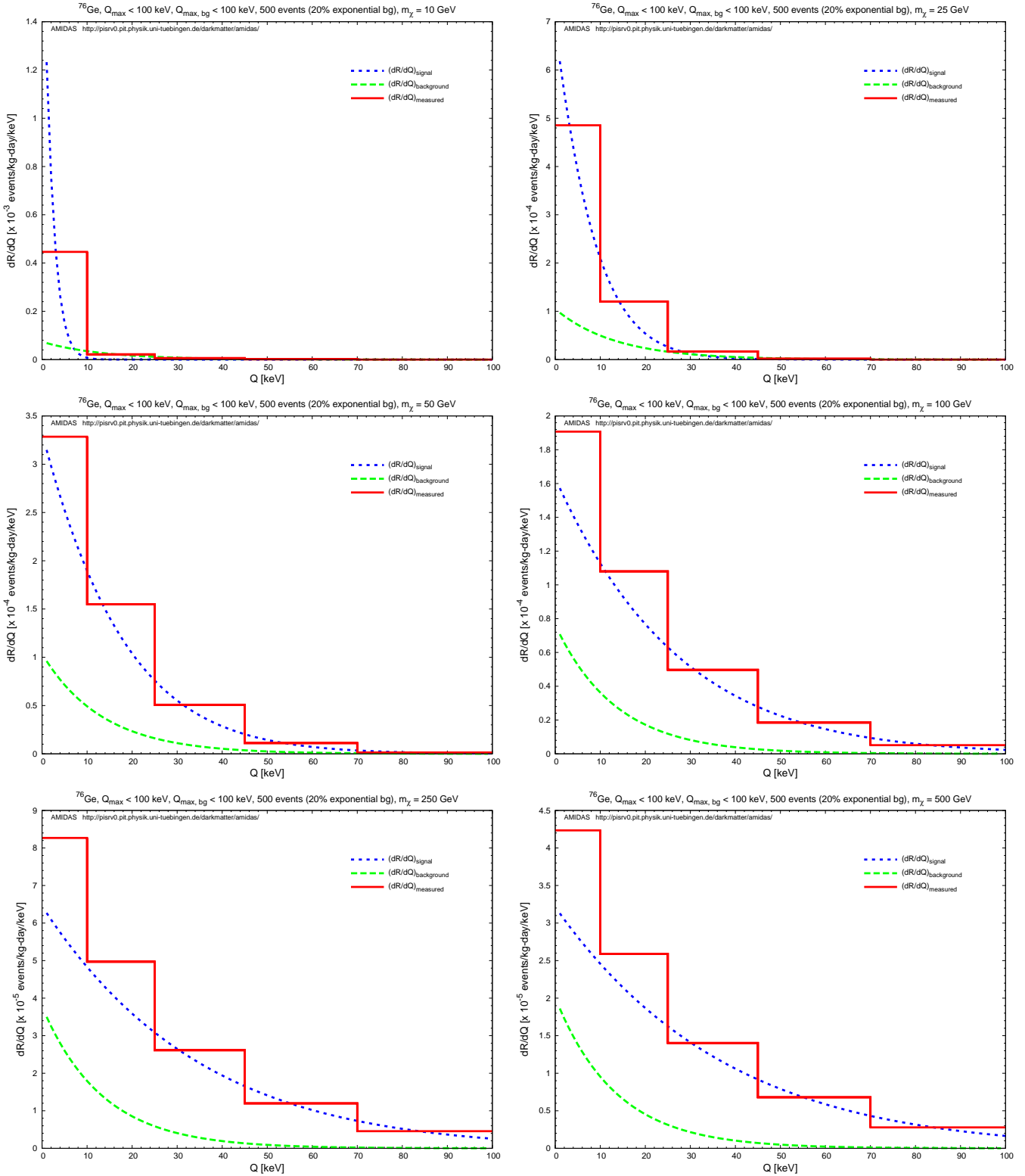


Figure 1: Measured energy spectra (solid red histograms) for a ^{76}Ge target with six different WIMP masses: 10, 25, 50, 100, 250, and 500 GeV. The dotted blue curves are the elastic WIMP–nucleus scattering spectra for the shifted Maxwellian velocity distribution and the Woods–Saxon elastic nuclear form factor; whereas the dashed green curves are the exponential background spectra normalized to fit to the chosen background ratio, which has been set as 20% here. The experimental threshold energy has been assumed to be negligible and the maximal cut–off energy is set as 100 keV. The background windows have been assumed to be the same as the experimental possible energy ranges. 5,000 experiments with 500 total events on average in each experiment have been simulated. See the text for further details.

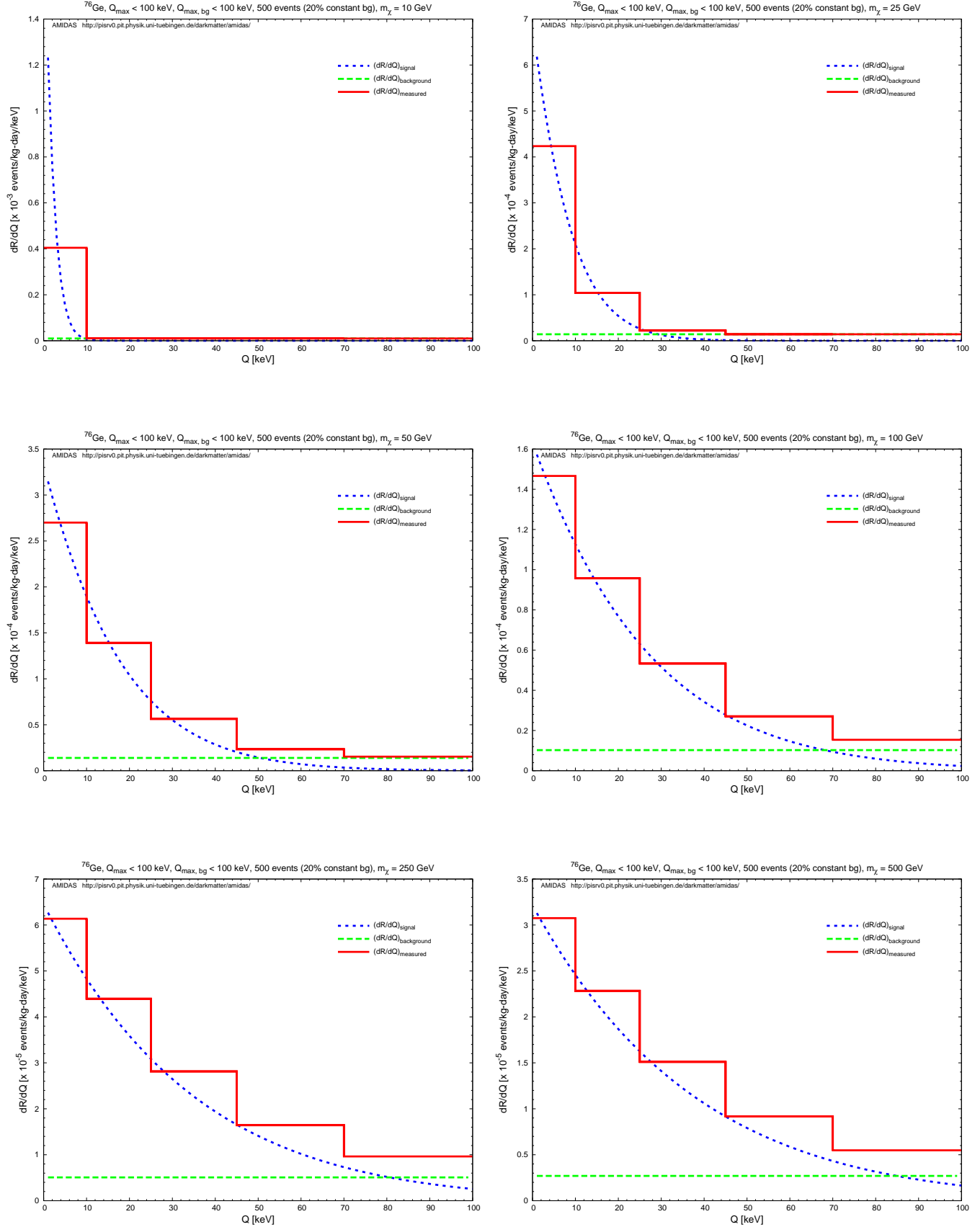


Figure 2: As in Figs. 1, except that the constant background spectrum in Eq. (13) has been used. See the text for further details.

target mass and are rather *flatter* (*sharper*) for *light* (*heavy*) WIMP masses compared to the WIMP scattering spectra. This means that, once input WIMPs are *light* (*heavy*), background events would contribute relatively more to *high* (*low*) energy ranges, and, consequently, the measured energy spectra would mimic scattering spectra induced by *heavier* (*lighter*) WIMPs.

As a comparison, in Figs. 2 we generate background events with the constant spectrum given in Eq. (13). It can be seen clearly that, since the background spectrum now is flatter for all WIMP masses, background events contribute always relatively more to *high* energy ranges, and, therefore, the measured energy spectra would always mimic scattering spectra induced by *heavier* WIMPs.

3 Reconstruction of the WIMP mass

In this section we first review the model-independent method for determining the WIMP mass introduced in Refs. [5, 6]. Then we demonstrate some numerical results of the reconstructed WIMP mass by using mixed data sets from WIMP signals and background events based on Monte Carlo simulations.

3.1 Model-independent determination of the WIMP mass

Here we review briefly the model-independent data analysis procedure for the determination of the WIMP mass by using two experimental data sets with different target nuclei. Detailed derivations and discussions can be found in Refs. [5, 6].

3.1.1 Basic expressions for determining the WIMP mass

In the earlier work [7], it was found that the normalized one-dimensional velocity distribution function of incident WIMPs can be solved from Eq. (1) directly and, consequently, its generalized moments can be estimated by [6]

$$\begin{aligned} \langle v^n \rangle(v(Q_{\min}), v(Q_{\max})) &= \int_{v(Q_{\min})}^{v(Q_{\max})} v^n f_1(v) dv \\ &= \alpha^n \left[\frac{2Q_{\min}^{(n+1)/2} r(Q_{\min})/F^2(Q_{\min}) + (n+1)I_n(Q_{\min}, Q_{\max})}{2Q_{\min}^{1/2} r(Q_{\min})/F^2(Q_{\min}) + I_0(Q_{\min}, Q_{\max})} \right]. \end{aligned} \quad (15)$$

Here $v(Q) = \alpha\sqrt{Q}$, $Q_{(\min, \max)}$ are the experimental minimal and maximal cut-off energies,

$$r(Q_{\min}) \equiv \left(\frac{dR}{dQ} \right)_{\text{expt}, Q=Q_{\min}} \quad (16)$$

is an estimated value of the *measured* recoil spectrum $(dR/dQ)_{\text{expt}}$ (*before* the normalization by the exposure \mathcal{E}) at $Q = Q_{\min}$, and $I_n(Q_{\min}, Q_{\max})$ can be estimated through the sum:

$$I_n(Q_{\min}, Q_{\max}) = \sum_a \frac{Q_a^{(n-1)/2}}{F^2(Q_a)}, \quad (17)$$

where the sum runs over all events in the data set that satisfy $Q_a \in [Q_{\min}, Q_{\max}]$.

By requiring that the values of a given moment of $f_1(v)$ estimated by Eq. (15) from two experiments with different target nuclei, X and Y , agree, m_χ appearing in the prefactor α^n on the right-hand side of Eq. (15) has been solved as [5]:

$$m_\chi|_{\langle v^n \rangle} = \frac{\sqrt{m_X m_Y} - m_X(\mathcal{R}_{n,X}/\mathcal{R}_{n,Y})}{\mathcal{R}_{n,X}/\mathcal{R}_{n,Y} - \sqrt{m_X/m_Y}}, \quad (18)$$

where

$$\mathcal{R}_{n,X} \equiv \left[\frac{2Q_{\min,X}^{(n+1)/2} r_X(Q_{\min,X})/F_X^2(Q_{\min,X}) + (n+1)I_{n,X}}{2Q_{\min,X}^{1/2} r_X(Q_{\min,X})/F_X^2(Q_{\min,X}) + I_{0,X}} \right]^{1/n}, \quad (19)$$

and $\mathcal{R}_{n,Y}$ can be defined analogously. Here $n \neq 0$, $m_{(X,Y)}$ and $F_{(X,Y)}(Q)$ are the masses and the form factors of the nucleus X and Y , respectively, and $r_{(X,Y)}(Q_{\min,(X,Y)})$ refer to the counting rates for detectors X and Y at the respective lowest recoil energies included in the analysis. Note that, firstly, the general expression (18) can be used either for spin-independent or for spin-dependent scattering, one only needs to choose different form factors under different assumptions. Secondly, the form factors in the estimate of $I_{n,X}$ and $I_{n,Y}$ using Eq. (17) are also different.

On the other hand, by using the theoretical prediction that the SI WIMP-nucleus cross section dominates, and the fact that the integral over the one-dimensional WIMP velocity distribution on the right-hand side of Eq. (1) is the minus-first moment of this distribution, which can be estimated by Eq. (15) with $n = -1$, one can easily find that [6]

$$\rho_0 |f_p|^2 = \frac{\pi}{4\sqrt{2}} \left(\frac{m_\chi + m_N}{\mathcal{E} A^2 \sqrt{m_N}} \right) \left[\frac{2Q_{\min}^{1/2} r(Q_{\min})}{F^2(Q_{\min})} + I_0 \right]. \quad (20)$$

Note that the exposure of the experiment, \mathcal{E} , appears in the denominator. Since the unknown factor $\rho_0 |f_p|^2$ on the left-hand side above is identical for different targets, it leads to a second expression for determining m_χ [6]:

$$m_\chi|_\sigma = \frac{(m_X/m_Y)^{5/2} m_Y - m_X(\mathcal{R}_{\sigma,X}/\mathcal{R}_{\sigma,Y})}{\mathcal{R}_{\sigma,X}/\mathcal{R}_{\sigma,Y} - (m_X/m_Y)^{5/2}}. \quad (21)$$

Here $m_{(X,Y)} \propto A_{(X,Y)}$ has been assumed,

$$\mathcal{R}_{\sigma,X} \equiv \frac{1}{\mathcal{E}_X} \left[\frac{2Q_{\min,X}^{1/2} r_X(Q_{\min,X})}{F_X^2(Q_{\min,X})} + I_{0,X} \right], \quad (22)$$

and similarly for $\mathcal{R}_{\sigma,Y}$.

3.1.2 χ^2 -fitting

In order to yield the best-fit WIMP mass as well as to minimize its statistical uncertainty by combining the estimators for different n in Eq. (18) with each other and with the estimator in Eq. (21), a χ^2 function has been introduced as [6]

$$\chi^2(m_\chi) = \sum_{i,j} (f_{i,X} - f_{i,Y}) \mathcal{C}_{ij}^{-1} (f_{j,X} - f_{j,Y}), \quad (23)$$

where

$$f_{i,X} \equiv \alpha_X^i \left[\frac{2Q_{\min,X}^{(i+1)/2} r_X(Q_{\min})/F_X^2(Q_{\min,X}) + (i+1)I_{i,X}}{2Q_{\min,X}^{1/2} r_X(Q_{\min})/F_X^2(Q_{\min,X}) + I_{0,X}} \right] \left(\frac{1}{300 \text{ km/s}} \right)^i, \quad (24a)$$

for $i = -1, 1, 2, \dots, n_{\max}$, and

$$f_{n_{\max}+1,X} \equiv \mathcal{E}_X \left[\frac{A_X^2}{2Q_{\min,X}^{1/2} r_X(Q_{\min}) / F_X^2(Q_{\min,X}) + I_{0,X}} \right] \left(\frac{\sqrt{m_X}}{m_\chi + m_X} \right); \quad (24b)$$

the other $n_{\max} + 2$ functions $f_{i,Y}$ can be defined analogously. Here n_{\max} determines the highest moment of $f_1(v)$ that is included in the fit. The f_i are normalized such that they are dimensionless and very roughly of order unity in order to alleviate numerical problems associated with the inversion of their covariance matrix. Note that the first $n_{\max} + 1$ fit functions depend on m_χ only through the overall factor α and that m_χ in Eqs. (24a) and (24b) is now a fit parameter, which may differ from the true value of the WIMP mass. Finally, \mathcal{C} in Eq. (23) is the total covariance matrix. Since the X and Y quantities are statistically completely independent, \mathcal{C} can be written as a sum of two terms:

$$\mathcal{C}_{ij} = \text{cov}(f_{i,X}, f_{j,X}) + \text{cov}(f_{i,Y}, f_{j,Y}). \quad (25)$$

3.1.3 Matching the cut-off energies

The basic requirement of the expressions for determining m_χ given in Eqs. (18) and (21) is that, from two experiments with different target nuclei, the values of a given moment of the WIMP velocity distribution estimated by Eq. (15) should agree. This means that the upper cuts on $f_1(v)$ in two data sets should be (approximately) equal⁶. Since $v_{\text{cut}} = \alpha\sqrt{Q_{\max}}$, it requires that [6]

$$Q_{\max,Y} = \left(\frac{\alpha_X}{\alpha_Y} \right)^2 Q_{\max,X}. \quad (26)$$

Note that α defined in Eq. (5) is a function of the true WIMP mass. Thus this relation for matching optimal cut-off energies can be used only if m_χ is already known. One possibility to overcome this problem is to fix the cut-off energy of the experiment with the heavier target, minimize the $\chi^2(m_\chi)$ function defined in Eq. (23), and then estimate the cut-off energy for the lighter nucleus by Eq. (26) algorithmically [6].

3.2 Reconstructing m_χ by using data sets with background events

In this subsection we show some numerical results of the reconstruction of the WIMP mass with mixed data sets from WIMP-induced and background events by means of the model-independent method described in the previous subsection. The upper and lower bounds on the reconstructed WIMP mass are estimated from the requirement that χ^2 exceeds its minimum by 1.⁷ As in Ref. [6], ²⁸Si and ⁷⁶Ge have been chosen as two target nuclei. The scattering cross section σ_0 in Eq. (2) has been assumed to be dominated by the spin-independent WIMP-nucleus interaction. The experimental threshold energies of two experiments have been assumed to be negligible and the maximal cut-off energies are set the same as 100 keV. $2 \times 5,000$ experiments have been simulated. In order to avoid large contributions from very few events in high energy ranges to the higher moments [7], only the moments up to $n_{\max} = 2$ were included in the χ^2 fit.

⁶Here the threshold energies have been assumed to be negligibly small.

⁷Note that, rather than the mean values, the (bounds on the) reconstructed WIMP mass are always the *median* values of the simulated results.

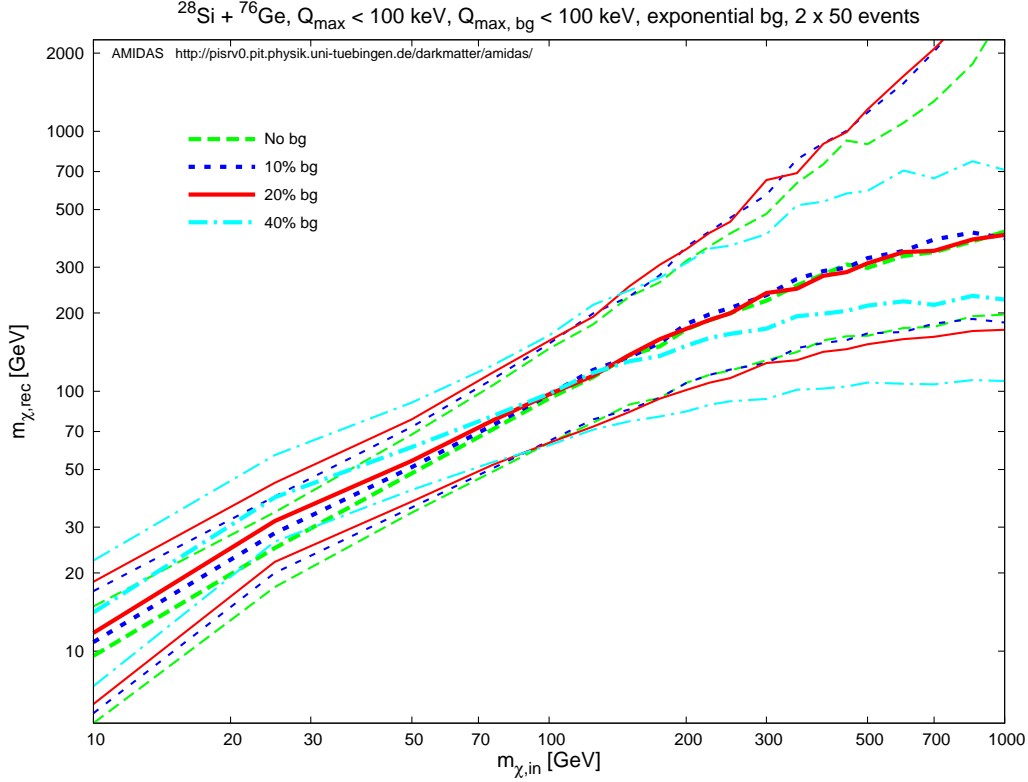


Figure 3: The reconstructed WIMP mass and the lower and upper bounds of the 1σ statistical uncertainty with mixed data sets from WIMP-induced and background events as functions of the input WIMP mass. ^{28}Si and ^{76}Ge have been chosen as two target nuclei. The background ratios shown here are no background (dashed green curves), 10% (long-dotted blue curves), 20% (solid red curves), and 40% (dash-dotted cyan curves) background events in the whole data sets in the experimental energy ranges between 0 and 100 keV. Each experiment contains 50 *total* events on average before cuts on Q_{max} for the experiments with the Si target; *all* of these events are treated as WIMP signals. Other parameters are as in Figs. 1. See the text for further details.

3.2.1 With the exponential background spectrum

Fig. 3 shows the reconstructed WIMP mass and the lower and upper bounds of the 1σ statistical uncertainty with mixed data sets from WIMP-induced and background events as functions of the input WIMP mass. As in Figs. 1, the exponential background spectrum has been used and the background windows are set as the same as the experimental possible energy ranges, i.e., between 0 and 100 keV for both experiments. The background ratios shown here are no background (dashed green curves), 10% (long-dotted blue curves), 20% (solid red curves), and 40% (dash-dotted cyan curves) background events in the whole data sets. Each experiment contains 50 *total* events on average before cuts on Q_{max} for the experiments with the Si target. Remind that *all* events recorded in our data sets are treated as WIMP signals in the analysis, although statistically we know that a fraction of these events could be backgrounds.

It can be seen clearly that, for *light* WIMP masses ($m_{\chi} \lesssim 100$ GeV), the larger the fraction of background events in the data sets, the *heavier* the reconstructed WIMP masses as well as the statistical uncertainty intervals. This is caused directly by the background contribution to *high* energy ranges shown in Figs. 1. As discussed in Sec. 2.3, the background spectrum is relatively *flatter* compared to the scattering spectrum induced by *light* WIMPs, and the energy spectrum of all recorded events would thus mimic a scattering spectrum induced by

WIMPs with a *relatively heavier* mass. Not surprisingly, the larger the background ratio, the more the background contribution to high energy ranges, and, consequently, the more strongly *overestimated* the reconstructed WIMP masses as well as the statistical uncertainty intervals.

In contrast, for *heavy* WIMP masses ($m_\chi \gtrsim 100$ GeV), Fig. 3 does not show very clearly but a tendency⁸ that the larger the fraction of background events, the *lighter* the reconstructed WIMP masses as well as the statistical uncertainty intervals. This is now caused by the background contribution to *low* energy ranges shown in Figs. 1. As discussed in the previous section, the background spectrum is relatively *sharper* compared to the scattering spectrum induced by *heavy* WIMPs, and the energy spectrum of all recorded events would thus mimic a scattering spectrum induced by WIMPs with a *relatively lighter* mass. Moreover, the larger the background ratio, the more the background contribution to low energy ranges, and, consequently, the more strongly *underestimated* the reconstructed WIMP masses as well as the statistical uncertainty intervals.

Nevertheless, from Fig. 3 it can be found that, with $\sim 20\%$ residue background events in the analyzed data sets, the true values of the WIMP mass can still fall in the middle of the 1σ statistical uncertainty band and one could thus in principle reconstruct the WIMP mass pretty well; if WIMPs are light ($m_\chi \lesssim 200$ GeV), the maximal acceptable fraction of residue background events could even be as large as $\sim 40\%$. For a WIMP mass of 100 GeV with 20% background events in the data sets, the reconstructed WIMP mass and the statistical uncertainty are $\sim 97 \text{ GeV}^{+61\%}_{-35\%}$, compared to $\sim 94 \text{ GeV}^{+55\%}_{-33\%}$ for background-free data sets; for a lighter WIMP mass of 50 GeV, the reconstructed WIMP mass and the statistical uncertainty change from $\sim 48 \text{ GeV}^{+41\%}_{-29\%}$ (background-free), to $\sim 54 \text{ GeV}^{+44\%}_{-30\%}$ (20% background), and $\sim 61 \text{ GeV}^{+48\%}_{-32\%}$ (40% background).

On the other hand, considering different efficiencies of discrimination ability against different background sources in different energy ranges in different experiments, in Figs. 4 we shrink the background window in each experiment to a relatively lower range between 0 and 50 keV (upper) and a relatively higher range between 50 and 100 keV (lower)⁹. Since our background spectrum is exponential, for the case shown in Fig. 3, only very few background events could be observed in the energy range between 50 and 100 keV. Hence, for the case with the background window only in the *low* energy range, not surprisingly, the results of the reconstructed WIMP mass shown in the upper frame of Figs. 4 should not differ very much from those shown in Fig. 3. However, due to the little bit more contribution to the *low* energy range from background events, *all* the reconstructed WIMP masses shown here are somehow *lighter* than those shown in Fig. 3. Hence, with $\sim 20\%$ residue background events in low experimental possible energy ranges, one could in principle reconstruct the WIMP mass with a 1σ statistical uncertainty as $\sim 94 \text{ GeV}^{+59\%}_{-34\%}$ (for a WIMP mass of 100 GeV) or $\sim 52 \text{ GeV}^{+44\%}_{-30\%}$ (for a WIMP mass of 50 GeV).

In contrast, since the WIMP scattering spectrum is in principle approximately exponential and thus only (very) few WIMP-induced events could be observed in high energy ranges, if we have background windows in only high experimental possible energy ranges, the (pretty large) contributions from background events could cause (strong) *overestimates* of the reconstructed WIMP masses. It is even worse for large WIMP masses ($m_\chi \gtrsim 100$ GeV)¹⁰. Nevertheless, as shown in the lower frame of Figs. 4, with $\sim 5\%$ residue background events observed only in

⁸Since for heavy input WIMP masses the reconstructed values are *systematically underestimated*, probably due to the statistical fluctuation with pretty few (~ 50) events discussed later.

⁹Note that here we do *not* mean that in other energy ranges background events do not exist; in contrast, we want to study what could happen once our background discrimination, caused by some natural or even artificial reasons, are *worse* in these energy ranges than others and *more* background events could thus survive.

¹⁰Note that the plateau of the lower bound of the statistical uncertainty in the case of a 10% background ratio for heavy WIMP masses ($m_\chi \gtrsim 300$ GeV) should be caused by our setup for the upper cut-off of the reconstructed WIMP mass of 3000 GeV in the simulations.

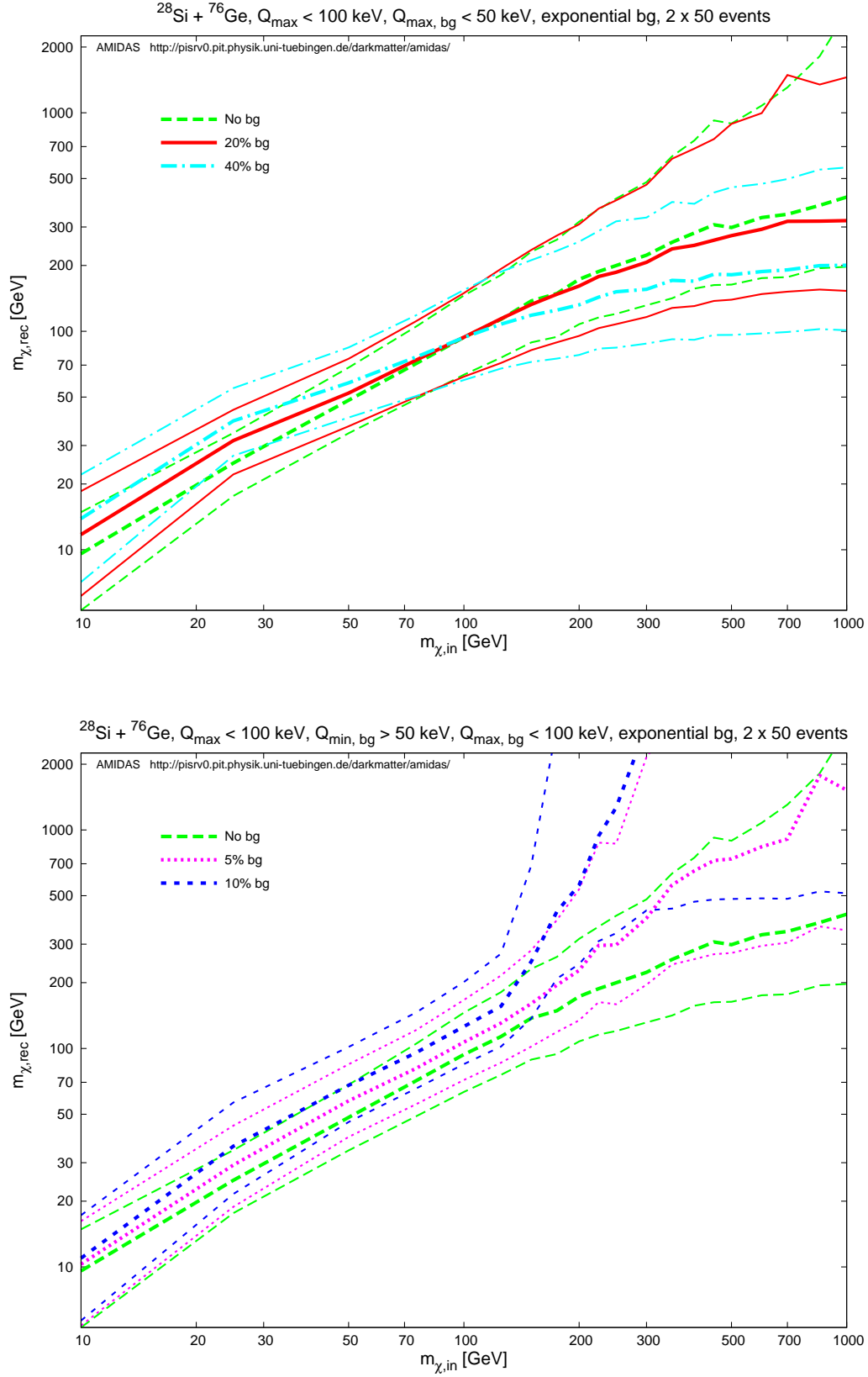


Figure 4: As in Fig. 3, except that the background window in each experiment have been set as $0 - 50 \text{ keV}$ (upper) and $50 - 100 \text{ keV}$ (lower). Note that the background ratios shown here are 20% (solid red curves) and 40% (dash-dotted cyan curves) in the upper frame, whereas 5% (dotted magenta curves) and 10% (long-dotted blue curves) in the lower frame.

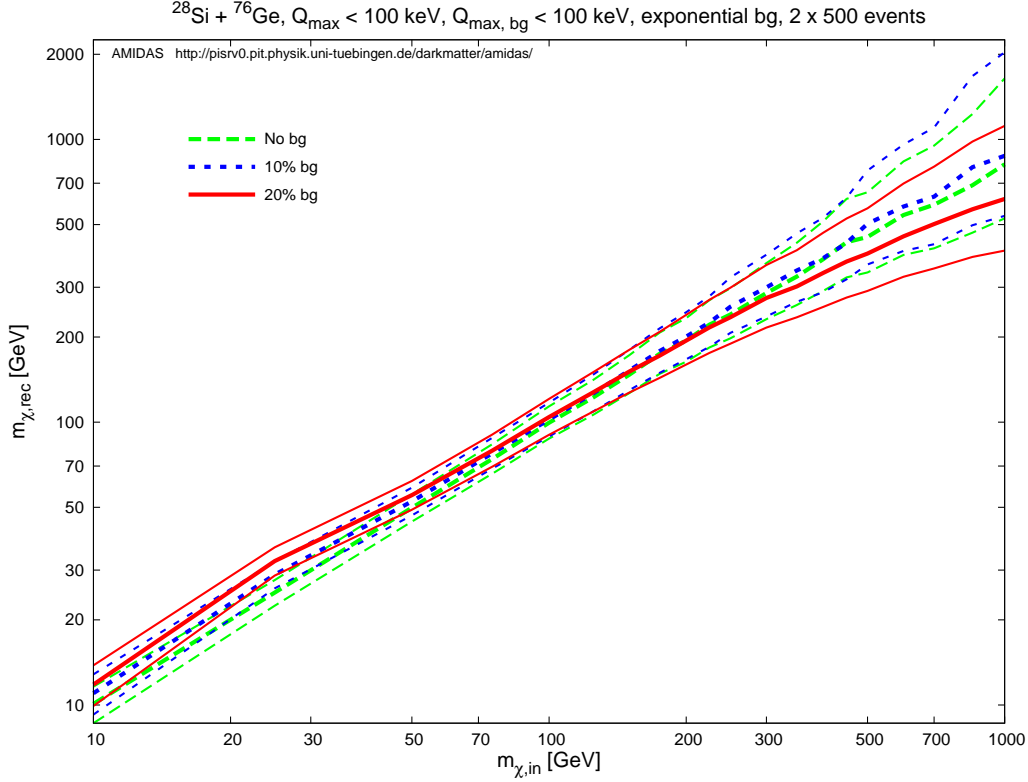


Figure 5: As in Fig. 3, except that the expected number of total events in each experiment has been set as 500.

high energy ranges, one could in principle still estimate the WIMP mass with a 1σ statistical uncertainty as $\sim 107 \text{ GeV}^{+56\%}_{-33\%}$ (for an input WIMP mass of 100 GeV) or $\sim 58 \text{ GeV}^{+47\%}_{-32\%}$ (for an input WIMP mass of 50 GeV).

Our results shown in Figs. 4 indicate that a small fraction of background events in *low* energy ranges might not affect the reconstructed WIMP mass significantly. However, the WIMP mass could be (strongly) *overestimated* once the same (or even smaller) amount of background events exists in *high* energy ranges. In practice one simple way to reduce the overestimate induced by an excess of background events in high energy ranges might be checking the shape of measured recoil spectrum. However, considering some suggested modifications of the standard shifted Maxwellian velocity distribution, e.g., contributions from discrete “streams” with (nearly) fixed velocities [22, 23, 24] or the “late infall” component in the velocity distribution with a velocity $v \sim v_{\text{esc}}$ [22, 25, 24], it should at least be very careful to reject any recoil event observed in high energy ranges artificially.

In Fig. 5 we rise the expected number of total events in each experiment by a factor of 10, to 500 events on average before cuts for the case that residue background events exist in the entire experimental possible energy ranges. As shown here, all statistical uncertainties shrink by a factor $\gtrsim 3$ compared to the results shown in Fig. 3. In addition, the underestimate of the reconstructed values of heavy input WIMP masses caused perhaps by the use of pretty few (~ 50) events has been reduced with larger data sets; and, the tendency of the underestimate of the reconstructed WIMP mass for heavy WIMP masses ($m_{\chi} \gtrsim 100 \text{ GeV}$) becomes more clearly. Finally, Fig. 5 shows that, for the determination of the WIMP mass by using data sets of $\mathcal{O}(500)$ total events, the maximal acceptable background ratio could be $\sim 10\%$ (i.e., $\mathcal{O}(50)$ background events) or even $\sim 20\%$, if WIMPs have a mass of $\mathcal{O}(100 \text{ GeV})$.

3.2.2 Statistical fluctuation

As discussed in Ref. [6], the statistical fluctuation of the reconstructed WIMP mass by the algorithmic procedure in the simulated experiments seems to be pretty problematic, in particular for heavier input WIMP masses. Moreover, as mentioned in the previous subsection, with only ~ 50 total events in each experiment, the tendency of the underestimate of the reconstructed WIMP mass for heavier WIMP masses ($m_\chi \gtrsim 100$ GeV) seems not to be very clear. Hence, as done in Ref. [6], in order to study the statistical fluctuation of the reconstructed WIMP mass with different background ratios in our data sets, we consider in this subsection the estimator δm introduced in Ref. [6]:

$$\delta m = \begin{cases} 1 + \frac{m_{\chi, \text{lo1}} - m_{\chi, \text{in}}}{m_{\chi, \text{lo1}} - m_{\chi, \text{lo2}}}, & \text{if } m_{\chi, \text{in}} \leq m_{\chi, \text{lo1}}; \\ \frac{m_{\chi, \text{rec}} - m_{\chi, \text{in}}}{m_{\chi, \text{rec}} - m_{\chi, \text{lo1}}}, & \text{if } m_{\chi, \text{lo1}} < m_{\chi, \text{in}} < m_{\chi, \text{rec}}; \\ \frac{m_{\chi, \text{rec}} - m_{\chi, \text{in}}}{m_{\chi, \text{hi1}} - m_{\chi, \text{rec}}}, & \text{if } m_{\chi, \text{rec}} < m_{\chi, \text{in}} < m_{\chi, \text{hi1}}; \\ \frac{m_{\chi, \text{hi1}} - m_{\chi, \text{in}}}{m_{\chi, \text{hi2}} - m_{\chi, \text{hi1}}} - 1, & \text{if } m_{\chi, \text{in}} \geq m_{\chi, \text{hi1}}. \end{cases} \quad (27)$$

Here $m_{\chi, \text{in}}$ is the true (input) WIMP mass, $m_{\chi, \text{rec}}$ its reconstructed value, $m_{\chi, \text{lo1}(2)}$ are the $1(2)\sigma$ lower bounds satisfying $\chi^2(m_{\chi, \text{lo}(1,2)}) = \chi^2(m_{\chi, \text{rec}}) + 1(4)$, and $m_{\chi, \text{hi1}(2)}$ are the corresponding $1(2)\sigma$ upper bounds.

The estimator δm defined above indicates basically the *strength of the deviation* of the reconstructed WIMP mass from the true (input) value. If the reconstructed 1σ lower and upper bounds on the WIMP mass in one simulated experiment cover the true value: $m_{\chi, \text{lo1}} \leq m_{\chi, \text{in}} \leq m_{\chi, \text{hi1}}$, δm is determined as the deviation of the “reconstructed WIMP mass” from the true one in units of the difference between the reconstructed value and the 1σ lower (upper) bound, once the reconstructed value is overestimated (underestimated). However, if the true WIMP mass lies *outside* of the experimental 1σ bounds (the reconstructed value is more strongly over-/underestimated), δm is determined as the deviation of the “ 1σ lower (upper) bound” from the true WIMP mass in units of the difference between the 1σ and 2σ lower (upper) bounds. Note that, it has been found in Ref. [6] as well as in the results presented in the previous subsection that the uncertainty intervals of the median reconstructed WIMP mass are quite asymmetric; similarly, the distance between the 1σ and 2σ bounds can be quite different from the distance between the reconstructed value and the 1σ bound [6]. The definition of δm in Eq.(27) takes these differences into account, and also keeps track of the sign of the deviation: if the reconstructed WIMP mass is overestimated (underestimated), δm is positive (negative). Moreover, $|\delta m| \leq 1(2)$ if and only if the true WIMP mass lies between the experimental $1(2)\sigma$ bounds.

In Figs. 6 we show the normalized distributions of the estimator δm defined in Eq. (27) for a rather heavy input WIMP mass of 200 GeV with 50 (upper) and 500 (lower) total events on average before cuts in each experiment. As discussed in Ref. [6], the deviation of the reconstructed WIMP mass in the simulated experiments looks asymmetric and non-Gaussian. However, it can be seen here clearly that, the more the background events in our analyzed data sets, the more concentrated the δm value in the range between -1 and 0 as well as between 0 and $+1$. Moreover, for the case with rather larger data sets of 500 total events, by increasing the background ratio the distribution becomes to be more symmetric and Gaussian-like, although the central

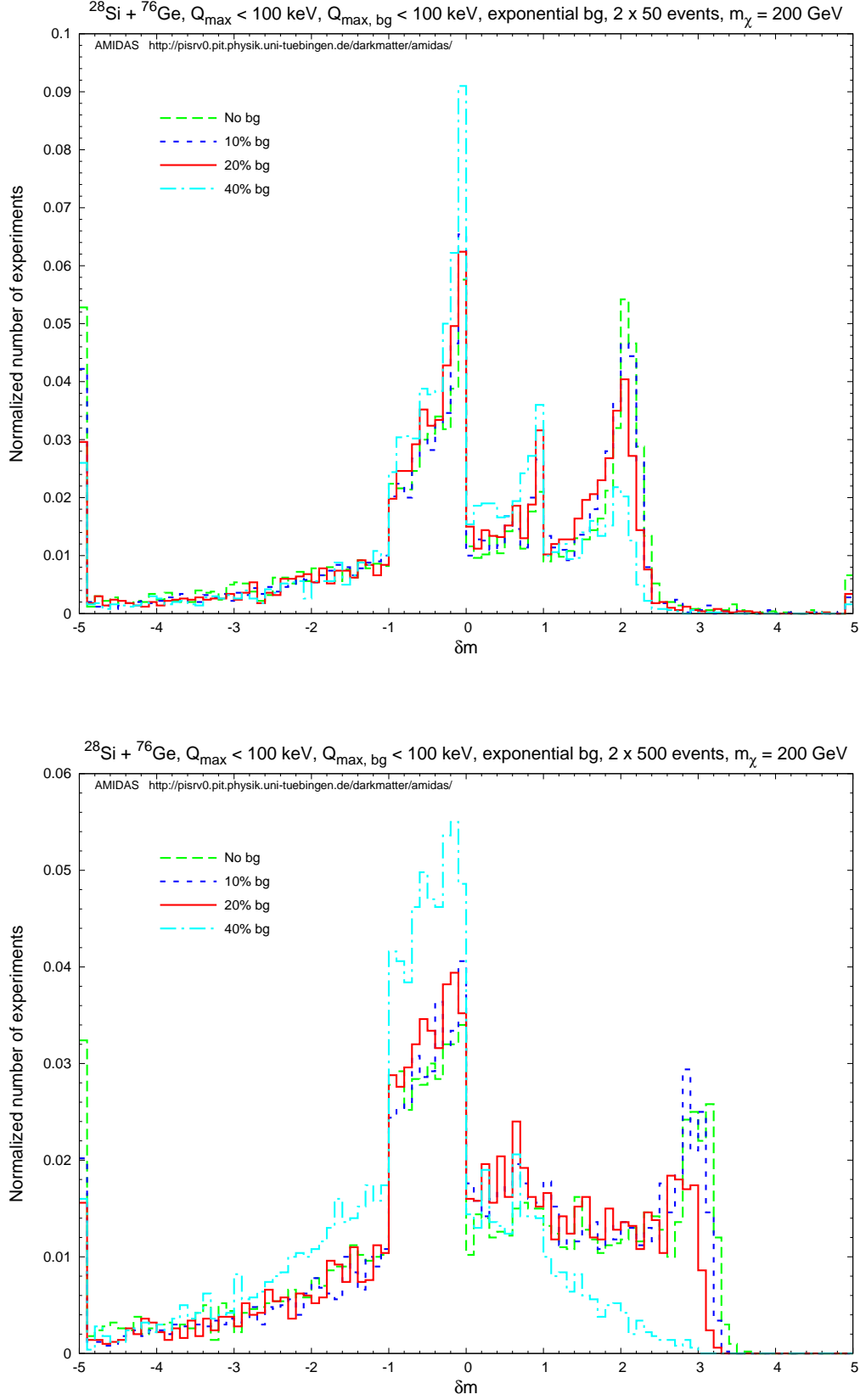


Figure 6: Normalized distributions of the estimator δm defined in Eq. (27) for an input WIMP mass of 200 GeV with 50 (upper) and 500 (lower) total events on average before cuts in each experiment. Parameters and notations are as in Fig. 3. Note that the bins at $\delta m = \pm 5$ are overflow bins, i.e., they also contain all experiments with $|\delta m| > 5$. See the text for further details.

value of δm seems to fall at ~ -0.5 because of the underestimate of the reconstructed WIMP mass.

In Ref. [6] it has been mentioned that with increasing number of total events the distribution of the estimator δm becomes slowly Gaussian. Figs. 6 here (and Fig. 9 shown later also) indicate that with a *larger* background ratio in the analyzed data sets the distribution of δm approaches to be Gaussian *more fast*. This interesting observation might be able to offer some new ideas for improving the algorithmic procedure for the reconstruction of the WIMP mass with a higher statistical certainty.

3.2.3 With the constant background spectrum

In order to check the need of a prior knowledge about an (exact) form of the residue background spectrum, we consider briefly in this subsection a rather extrem case, i.e., the constant background spectrum in Eq. (13).

In Fig. 7 we show the reconstructed WIMP mass and the lower and upper bounds of the 1σ statistical uncertainty with mixed data sets as functions of the input WIMP mass. As in Figs. 2, the windows of the constant background spectrum are set as the same as the experimental possible energy ranges, i.e., between 0 and 100 keV for both experiments. The background ratios shown here are no background (dashed green curves), 5% (dotted magenta curves), and 10% (long-dotted blue curves) background events in the whole data sets. Each experiment contains again 50 total events on average before cuts; all of these events are treated as WIMP signals in the analysis.

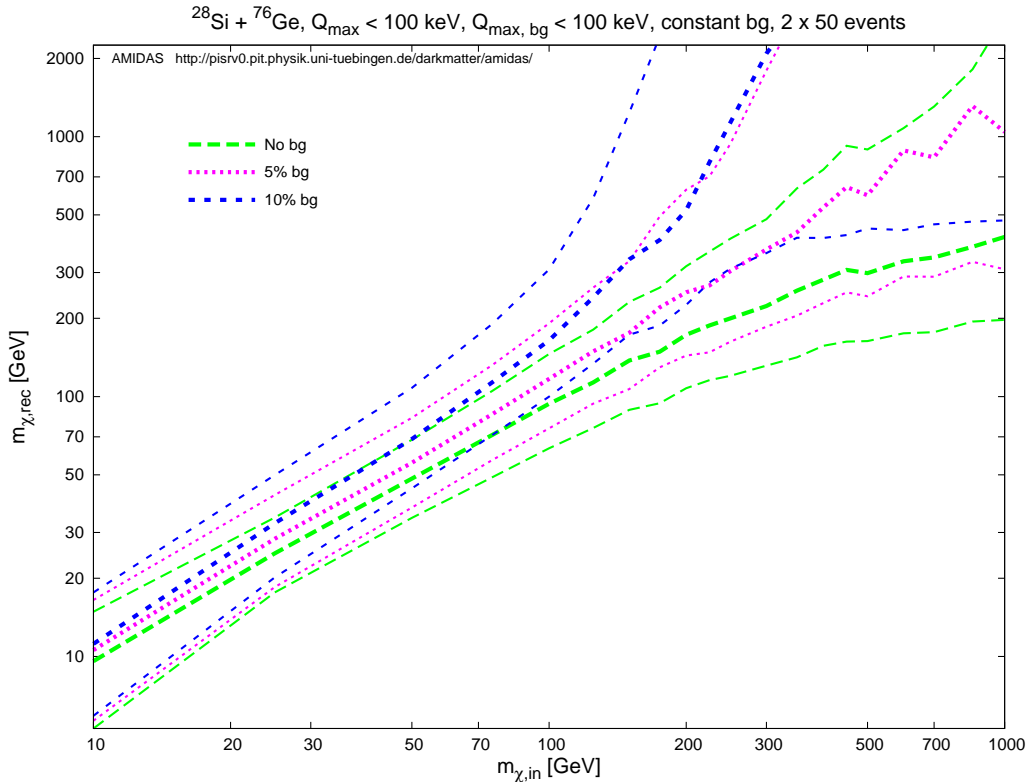


Figure 7: As in Fig. 3, except that the constant background spectrum in Eq. (13) has been used. Note that the background ratios shown here are 5% (dotted magenta curves) and 10% (long-dotted blue curves).

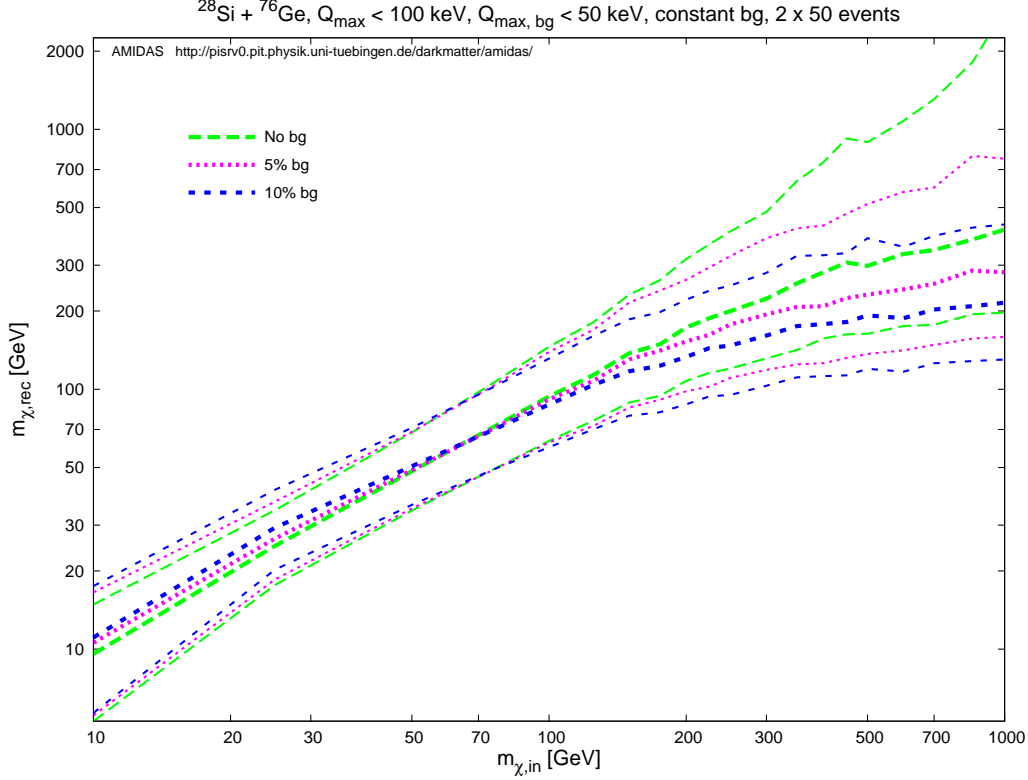


Figure 8: As in Fig. 7, except that the background window in each experiment has been set as 0 – 50 keV.

It can be seen clearly that, as discussed above, since the constant background spectrum has relatively *flatter* shape compared to the WIMP scattering spectrum for not only light, but also heavy WIMP masses, and the measured energy spectrum should thus always mimic a scattering spectrum induced by *heavier* WIMPs, the reconstructed WIMP masses are therefore *overestimated* for all input WIMP masses, especially for the heavier masses. Actually, the result shown here looks more likely that shown in the lower frame of Figs. 4, since in both cases residue background events contribute significantly more (compared to the exponential-like WIMP scattering spectrum) in high energy ranges. Not surprisingly, the larger the background ratio, the more strongly overestimated the reconstructed WIMP masses, in particular for the heavier input WIMP masses. Nevertheless, for (approximately) constant residue backgrounds with a fraction of $\sim 5\%$ in background windows as the entire experimental possible ranges, one could in principle still estimate the WIMP mass with a 1σ statistical uncertainty as $\sim 117 \text{ GeV}^{+64\%}_{-35\%}$ (for 100 GeV WIMPs) or $\sim 56 \text{ GeV}^{+49\%}_{-33\%}$ (for 50 GeV WIMPs). Once WIMPs are light ($m_\chi \sim \mathcal{O}(25 \text{ GeV})$), the maximal acceptable background ratio could even be $\sim 10\%$.

Moreover, as done in Sec. 3.2.1, in Fig. 8 we shrink the background window in each experiment to the lower energy range between 0 and 50 keV. Not surprisingly, while for light WIMPs ($m_\chi \lesssim 70 \text{ GeV}$)¹¹, relatively more background events still contribute to high energy ranges; for heavy WIMPs ($m_\chi \gtrsim 70 \text{ GeV}$), relatively more background events contribute now to low energy ranges and, consequently, the reconstructed WIMP masses are therefore *underestimated* for heavy WIMPs.

¹¹Remind that the actual value of this “critical” WIMP mass depends in practice strongly on the WIMP scattering spectrum as well as on the residue background spectrum and therefore differs from experiment to experiment.

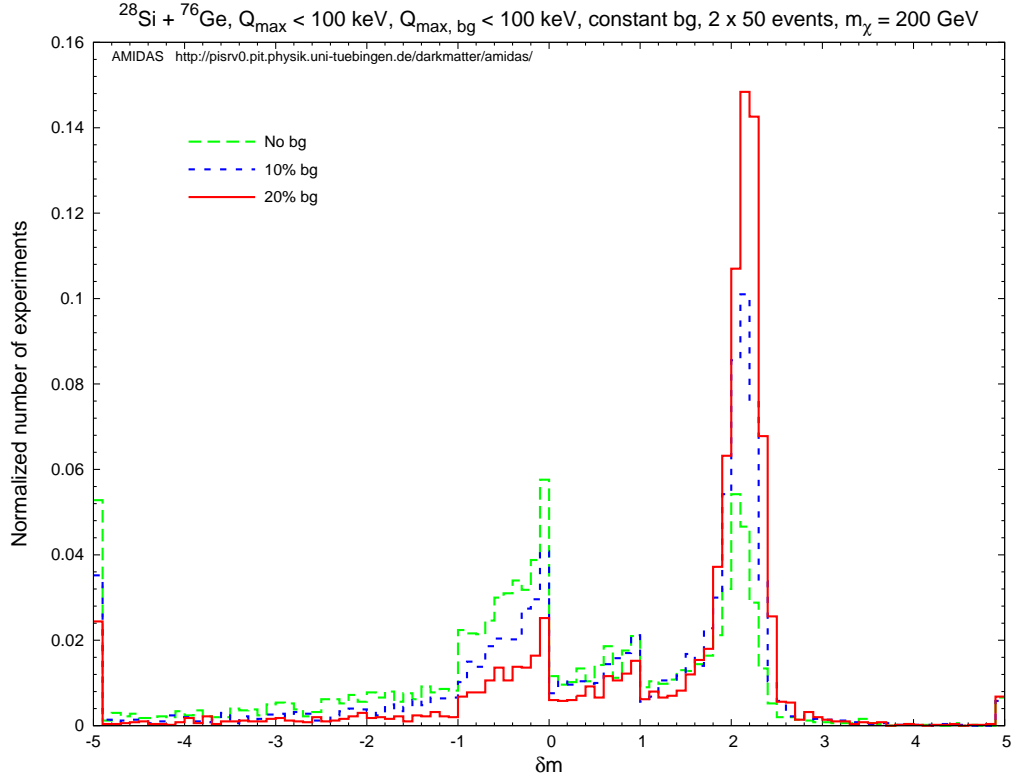


Figure 9: As in the upper frame of Figs. 6, except that the constant background spectrum in Eq. (13) has been used.

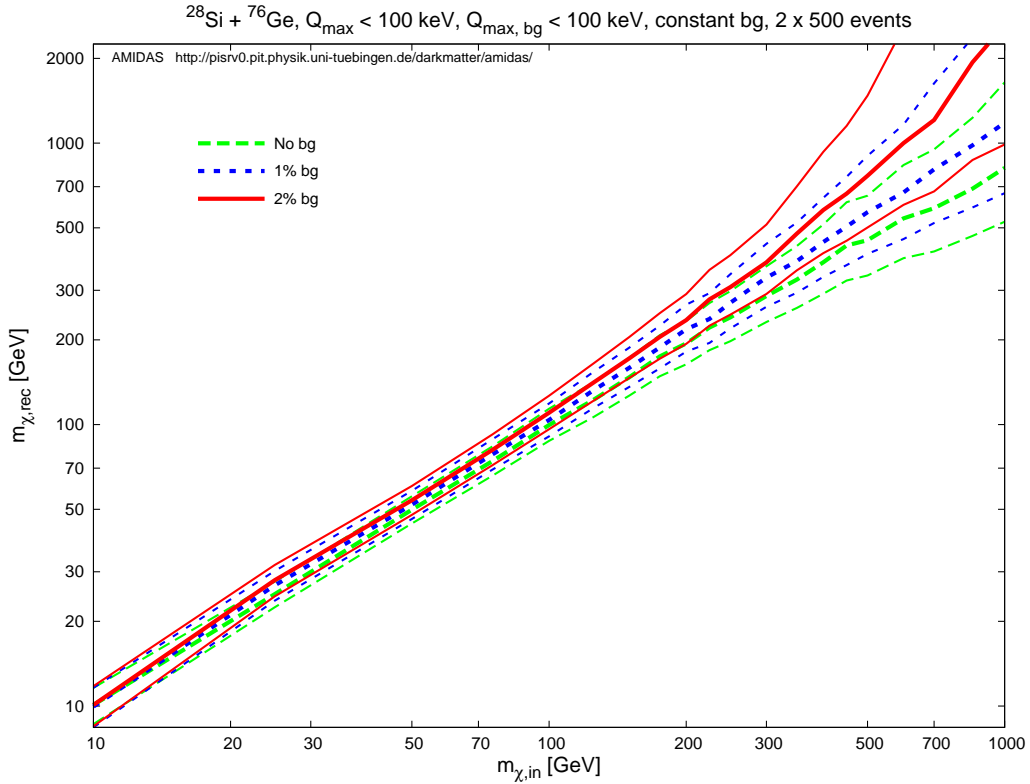


Figure 10: As in Fig. 7, except that the expected number of total events in both experiments has been set as 500. Note that the background ratios shown here are no background (dashed green curves), 1% (long-dotted blue curves), and 2% (solid red curves), i.e., a factor of 10 smaller than the ratios used before. See the text for further details.

On the other hand, as in Sec. 3.2.2, in Fig. 9 we check the normalized distributions of the estimator δm for an input WIMP mass of 200 GeV with 50 total events on average before cuts in each experiment. It can be seen very clearly that, with increasing background ratio the value of δm concentrates more and more strongly to 2. This means that, due to the contribution from residue background events, the reconstructed WIMP mass is most possibly $\sim 2\sigma$ overestimated. Moreover, compared to the non-Gaussian form of the distributions for the case with the exponential background spectrum shown in the upper frame of Figs. 6, the distributions with the constant spectrum look more likely Gaussian, despite of the asymmetry due to the overestimate of the WIMP mass. Nevertheless, Figs. 6 and Fig. 9 indicate that background events seem to let the distribution of the deviation of the reconstructed WIMP mass be more symmetric and Gaussian, no matter what kind of energy spectrum they would have.

Finally, in Fig. 10 we rise the expected number of total events in each experiment by a factor of 10, to 500 events on average before cuts for the case that residue background events exist in the entire experimental possible energy ranges. Note that the background ratios shown here are no background (dashed green curves), 1% (long-dotted blue curves), and 2% (solid red curves), i.e., a factor of 10 smaller than the ratios used before. In the lower frame of Figs. 4 and in Fig. 7, we found that once $\sim 5\% - 10\%$ events in our analyzed data sets are residue backgrounds and (most of) these events are recorded in high energy ranges, no matter what kind of spectrum shape they would have, the reconstructed WIMP mass could be (strongly) *overestimated*. However, Fig. 5 and Fig. 10 here show that, by increasing the event number and decreasing the background ratio, one could in principle determine the WIMP mass (pretty) precisely *without* knowing the (exact) form of the spectrum of residue background events.

4 Summary and conclusions

In this paper we reexamine the model-independent data analysis method introduced in Refs. [5, 6] for the determination of the mass of Weakly Interacting Massive Particles from data (measured recoil energies) of direct Dark Matter detection experiments directly by taking into account a fraction of residue background events, which pass all discrimination criteria and then mix with other real WIMP-induced events in the analyzed data sets. Differ from the maximum likelihood analysis described in Refs. [21, 14, 13], our method requires *neither* prior knowledge about the WIMP scattering spectrum *nor* about different possible background spectra; the unique needed information is the recoil energies recorded in *two* direct detection experiments with *two different* target nuclei.

In Sec. 2 we considered first the measured energy spectrum for different WIMP masses with two forms of possible residue background spectrum: the *target-dependent exponential* spectrum and the *constant* spectrum. The exponential background spectrum contributes relatively more events to *high* energy ranges once WIMPs are *light* ($m_\chi \lesssim 100$ GeV), and to *low* energy ranges for *heavy* WIMP masses ($m_\chi \gtrsim 100$ GeV); whereas the constant background spectrum contributes always relatively more events to *high* energy ranges. As the consequence, the energy spectrum of all observed events looks more likely to be a scattering spectrum induced by *heavier* WIMPs, once the spectrum of residue background events (induced perhaps by two or more different sources) is either exponential-like (and WIMPs are light) or approximately constant (for all WIMP masses); while if WIMPs are heavy and the residue background spectrum is approximately exponential, the measured energy spectrum would look more likely to be a scattering spectrum induced by *lighter* WIMPs.

In Sec. 3.2 the data sets generated in Sec. 2 have been analyzed for reconstructing the mass

of incident WIMPs by using the model-independent method. With the exponential background spectrum, the input WIMP mass would be *overestimated* once WIMPs are light ($m_\chi \lesssim 100$ GeV), or, in contrast, would be *underestimated* for heavy WIMPs ($m_\chi \gtrsim 100$ GeV). Our simulations show that, for background windows in the *entire or low* experimental possible energy ranges, one could in principle reconstruct the WIMP mass with a maximal fraction of $\sim 20\%$ of residue background events in the analyzed data sets; whereas for background windows in *high* energy ranges, the maximal acceptable fraction of residue backgrounds is only $\sim 10\%$.

Moreover, in order to check the need of a prior knowledge about an (exact) form of the residue background spectrum, we considered also the case with the constant background spectrum. In this rather extrem case, the WIMP mass would always be *overestimated*, especially for heavy WIMPs ($m_\chi \gtrsim 100$ GeV). Our simulations give then a maximal acceptable fraction of $\sim 5\% - 10\%$ of residue background events in the data sets for background windows in the *entire or low* experimental possible energy ranges. Nevertheless, we found also that, by means of increased number of observed (WIMP-induced) events and improved background discrimination techniques [9, 11], the WIMP mass could in principle be determined (pretty) precisely, no matter what kind of energy spectrum residue background events would have.

On the other hand, in order to check the statistical fluctuation of the reconstructed WIMP mass with increased background ratio, we considered also the distribution of the deviation of the reconstructed WIMP mass from the true value. It was found in Ref. [6] that, for a rather heavy WIMP mass of 200 GeV, the distribution of the deviation of the reconstructed WIMP mass is asymmetric and non-Gaussian, either with data sets of only a few ($\mathcal{O}(50)$) events or with larger data sets (of $\mathcal{O}(500)$ events). However, our simulations with different background ratios show that, firstly, for both used (exponential and constant) background spectra, with increasing background ratio the distribution of the deviation of the reconstructed WIMP mass becomes more and more concentrated, although still asymmetric and non-Gaussian. Secondly, for the more realistic exponential background spectrum and using data sets with a larger number of total events, with increasing background ratio the distribution of the deviation becomes somehow more symmetric and Gaussian. This observation might be able to offer some new ideas for improving the algorithmic procedure for the reconstruction of the WIMP mass with a higher statistical certainty.

In summary, our study of the effects of residue background events in direct Dark Matter detection experiments on the determination of the WIMP mass shows that, with currently running and projected experiments using detectors with 10^{-9} to 10^{-11} pb sensitivities [26, 27, 10, 28] and $< 10^{-6}$ background rejection ability [9, 11, 12, 8], once two or more experiments with different target nuclei could accumulate a few tens events (in one experiment), we could in principle already estimate the mass of Dark Matter particle with a reasonable precision, even though there might be some background events mixed in our data sets for the analysis¹². Moreover, two forms for background spectrum and three windows for residue background events considered in this work are rather naive. Nevertheless, one should be able to extend our observations/discussions to predict the effects of possible background events in their own experiment. Hopefully, this will encourage our experimental colleagues to present their (future) results not only in form of the “exclusion limit(s)”, but also of the “most possible area(s)” on the cross section versus mass plan.

¹²A possible first test could be a combination of the events observed by the CoGeNT experiment with their Ge detector with the events observed in the oxygen band of the CRESST-II experiment [29, 30, 31].

Acknowledgments

The authors would like to thank the Physikalisches Institut der Universität Tübingen for the technical support of the computational work demonstrated in this article. CLS would also like to thank the friendly hospitality of the Max-Planck-Institut für Kernphysik in Heidelberg where part of this work was completed. This work was partially supported by the National Science Council of R.O.C. under contracts no. NSC-96-2112-N-009-023-MY3 and no. NSC-98-2811-M-006-044 as well as by the LHC Physics Focus Group, National Center of Theoretical Sciences, R.O.C..

A Formulae needed in Sec. 3

Here we list all formulae needed for the model-independent data analyses procedure used in Sec. 3. Detailed derivations and discussions can be found in Refs. [7, 6].

A.1 Estimating $r(Q_{\min})$, $I_n(Q_{\min}, Q_{\max})$, and their statistical errors

Firstly, consider experimental data described by

$$Q_n - \frac{b_n}{2} \leq Q_{n,i} \leq Q_n + \frac{b_n}{2}, \quad i = 1, 2, \dots, N_n, \quad n = 1, 2, \dots, B. \quad (\text{A1})$$

Here the entire experimental possible energy range between Q_{\min} and Q_{\max} has been divided into B bins with central points Q_n and widths b_n . In each bin, N_n events will be recorded. Since the recoil spectrum dR/dQ is expected to be approximately exponential, the following ansatz for the *measured* recoil spectrum (*before* normalized by the exposure \mathcal{E}) in the n th bin has been introduced [7]:

$$\left(\frac{dR}{dQ}\right)_{\text{expt}, n} \equiv \left(\frac{dR}{dQ}\right)_{\text{expt}, Q \simeq Q_n} \equiv r_n e^{k_n(Q - Q_{s,n})}. \quad (\text{A2})$$

Here r_n is the standard estimator for $(dR/dQ)_{\text{expt}}$ at $Q = Q_n$:

$$r_n = \frac{N_n}{b_n}, \quad (\text{A3})$$

k_n is the logarithmic slope of the recoil spectrum in the n th Q -bin, which can be computed numerically from the average value of the measured recoil energies in this bin:

$$\overline{Q - Q_n}|_n = \left(\frac{b_n}{2}\right) \coth\left(\frac{k_n b_n}{2}\right) - \frac{1}{k_n}, \quad (\text{A4})$$

where

$$\overline{(Q - Q_n)^\lambda}|_n \equiv \frac{1}{N_n} \sum_{i=1}^{N_n} (Q_{n,i} - Q_n)^\lambda. \quad (\text{A5})$$

The error on the logarithmic slope k_n can be estimated from Eq. (A4) directly as

$$\sigma^2(k_n) = k_n^4 \left\{ 1 - \left[\frac{k_n b_n / 2}{\sinh(k_n b_n / 2)} \right]^2 \right\}^{-2} \sigma^2(\overline{Q - Q_n}|_n), \quad (\text{A6})$$

with

$$\sigma^2(\overline{Q - Q_n}|_n) = \frac{1}{N_n - 1} \left[\overline{(Q - Q_n)^2}|_n - \overline{Q - Q_n}|_n^2 \right]. \quad (\text{A7})$$

$Q_{s,n}$ in the ansatz (A2) is the shifted point at which the leading systematic error due to the ansatz is minimal [7],

$$Q_{s,n} = Q_n + \frac{1}{k_n} \ln \left[\frac{\sinh(k_n b_n/2)}{k_n b_n/2} \right]. \quad (\text{A8})$$

Note that $Q_{s,n}$ differs from the central point of the n th bin, Q_n . From the ansatz (A2), the counting rate at $Q = Q_{\min}$ can be calculated by

$$r(Q_{\min}) = r_1 e^{k_1(Q_{\min} - Q_{s,1})}, \quad (\text{A9})$$

and its statistical error can be expressed as

$$\sigma^2(r(Q_{\min})) = r^2(Q_{\min}) \left\{ \frac{1}{N_1} + \left[\frac{1}{k_1} - \left(\frac{b_1}{2} \right) \left(1 + \coth \left(\frac{b_1 k_1}{2} \right) \right) \right]^2 \sigma^2(k_1) \right\}, \quad (\text{A10})$$

since

$$\sigma^2(r_n) = \frac{N_n}{b_n^2}. \quad (\text{A11})$$

Finally, since all I_n are determined from the same data, they are correlated with

$$\text{cov}(I_n, I_m) = \sum_a \frac{Q_a^{(n+m-2)/2}}{F^4(Q_a)}, \quad (\text{A12})$$

where the sum runs again over all events with recoil energy between Q_{\min} and Q_{\max} . And the correlation between the errors on $r(Q_{\min})$, which is calculated entirely from the events in the first bin, and on I_n is given by

$$\begin{aligned} & \text{cov}(r(Q_{\min}), I_n) \\ &= r(Q_{\min}) I_n(Q_{\min}, Q_{\min} + b_1) \\ & \quad \times \left\{ \frac{1}{N_1} + \left[\frac{1}{k_1} - \left(\frac{b_1}{2} \right) \left(1 + \coth \left(\frac{b_1 k_1}{2} \right) \right) \right] \right. \\ & \quad \times \left. \left[\frac{I_{n+2}(Q_{\min}, Q_{\min} + b_1)}{I_n(Q_{\min}, Q_{\min} + b_1)} - Q_1 + \frac{1}{k_1} - \left(\frac{b_1}{2} \right) \coth \left(\frac{b_1 k_1}{2} \right) \right] \sigma^2(k_1) \right\}; \quad (\text{A13}) \end{aligned}$$

note that the sums I_i here only count in the first bin, which ends at $Q = Q_{\min} + b_1$.

A.2 Statistical errors on m_χ given in Eqs. (18) and (21)

By using the standard Gaussian error propagation, a lengthy expression for the statistical error on $m_\chi|_{\langle v^n \rangle}$ given in Eq. (18) can be obtained as

$$\begin{aligned} \sigma(m_\chi)|_{\langle v^n \rangle} &= \frac{\sqrt{m_X/m_Y} |m_X - m_Y| (\mathcal{R}_{n,X}/\mathcal{R}_{n,Y})}{(\mathcal{R}_{n,X}/\mathcal{R}_{n,Y} - \sqrt{m_X/m_Y})^2} \\ & \quad \times \left[\frac{1}{\mathcal{R}_{n,X}^2} \sum_{i,j=1}^3 \left(\frac{\partial \mathcal{R}_{n,X}}{\partial c_{i,X}} \right) \left(\frac{\partial \mathcal{R}_{n,X}}{\partial c_{j,X}} \right) \text{cov}(c_{i,X}, c_{j,X}) + (X \longrightarrow Y) \right]^{1/2}. \quad (\text{A14}) \end{aligned}$$

Here a short-hand notation for the six quantities on which the estimate of m_X depends has been introduced:

$$c_{1,X} = I_{n,X}, \quad c_{2,X} = I_{0,X}, \quad c_{3,X} = r_X(Q_{\min,X}); \quad (\text{A15})$$

and similarly for the $c_{i,Y}$. Estimators for $\text{cov}(c_i, c_j)$ have been given in Eqs. (A12) and (A13). Explicit expressions for the derivatives of $\mathcal{R}_{n,X}$ with respect to $c_{i,X}$ are:

$$\frac{\partial \mathcal{R}_{n,X}}{\partial I_{n,X}} = \frac{n+1}{n} \left[\frac{F_X^2(Q_{\min,X})}{2Q_{\min,X}^{(n+1)/2} r_X(Q_{\min,X}) + (n+1)I_{n,X} F_X^2(Q_{\min,X})} \right] \mathcal{R}_{n,X}, \quad (\text{A16a})$$

$$\frac{\partial \mathcal{R}_{n,X}}{\partial I_{0,X}} = -\frac{1}{n} \left[\frac{F_X^2(Q_{\min,X})}{2Q_{\min,X}^{1/2} r_X(Q_{\min,X}) + I_{0,X} F_X^2(Q_{\min,X})} \right] \mathcal{R}_{n,X}, \quad (\text{A16b})$$

and

$$\begin{aligned} \frac{\partial \mathcal{R}_{n,X}}{\partial r_X(Q_{\min,X})} &= \frac{2}{n} \left[\frac{Q_{\min,X}^{(n+1)/2} I_{0,X} - (n+1) Q_{\min,X}^{1/2} I_{n,X}}{2Q_{\min,X}^{(n+1)/2} r_X(Q_{\min,X}) + (n+1) I_{n,X} F_X^2(Q_{\min,X})} \right] \\ &\quad \times \left[\frac{F_X^2(Q_{\min,X})}{2Q_{\min,X}^{1/2} r_X(Q_{\min,X}) + I_{0,X} F_X^2(Q_{\min,X})} \right] \mathcal{R}_{n,X}; \end{aligned} \quad (\text{A16c})$$

explicit expressions for the derivatives of $\mathcal{R}_{n,Y}$ with respect to $c_{i,Y}$ can be given analogously. Note that, firstly, factors $\mathcal{R}_{n,(X,Y)}$ appear in all these expressions, which can practically be cancelled by the prefactors in the bracket in Eq. (A14). Secondly, all the $I_{0,(X,Y)}$ and $I_{n,(X,Y)}$ should be understood to be computed according to Eq. (17) with integration limits Q_{\min} and Q_{\max} specific for that target.

Similar to the analogy between Eqs. (18) and (21), the statistical error on $m_X|_\sigma$ given in Eq. (21) can be expressed as

$$\begin{aligned} \sigma(m_X)|_\sigma &= \frac{(m_X/m_Y)^{5/2} |m_X - m_Y| (\mathcal{R}_{\sigma,X}/\mathcal{R}_{\sigma,Y})}{\left[\mathcal{R}_{\sigma,X}/\mathcal{R}_{\sigma,Y} - (m_X/m_Y)^{5/2} \right]^2} \\ &\quad \times \left[\frac{1}{\mathcal{R}_{\sigma,X}^2} \sum_{i,j=2}^3 \left(\frac{\partial \mathcal{R}_{\sigma,X}}{\partial c_{i,X}} \right) \left(\frac{\partial \mathcal{R}_{\sigma,X}}{\partial c_{j,X}} \right) \text{cov}(c_{i,X}, c_{j,X}) + (X \rightarrow Y) \right]^{1/2}, \end{aligned} \quad (\text{A17})$$

where we have again used the short-hand notation in Eq. (A15); note that $c_{1,(X,Y)} = I_{n,(X,Y)}$ does not appear here. Expressions for the derivatives of $\mathcal{R}_{\sigma,X}$ can be computed from Eq. (22) as

$$\frac{\partial \mathcal{R}_{\sigma,X}}{\partial I_{0,X}} = \left[\frac{F_X^2(Q_{\min,X})}{2Q_{\min,X}^{1/2} r_X(Q_{\min,X}) + I_{0,X} F_X^2(Q_{\min,X})} \right] \mathcal{R}_{\sigma,X}, \quad (\text{A18a})$$

$$\frac{\partial \mathcal{R}_{\sigma,X}}{\partial r_X(Q_{\min,X})} = \left[\frac{2Q_{\min,X}^{1/2}}{2Q_{\min,X}^{1/2} r_X(Q_{\min,X}) + I_{0,X} F_X^2(Q_{\min,X})} \right] \mathcal{R}_{\sigma,X}; \quad (\text{A18b})$$

and similarly for the derivatives of $\mathcal{R}_{\sigma,Y}$.

A.3 Covariance of f_i defined in Eqs. (24a) and (24b)

The entries of the \mathcal{C} matrix given in Eq. (25) involving basically only the moments of the WIMP velocity distribution can be read off Eq. (82) of Ref. [7], with a slight modification due to the normalization factor in Eq. (24a)¹³:

$$\begin{aligned} \text{cov}(f_i, f_j) = \mathcal{N}_m^2 & \left[f_i f_j \text{cov}(I_0, I_0) + \tilde{\alpha}^{i+j} (i+1)(j+1) \text{cov}(I_i, I_j) \right. \\ & - \tilde{\alpha}^j (j+1) f_i \text{cov}(I_0, I_j) - \tilde{\alpha}^i (i+1) f_j \text{cov}(I_0, I_i) \\ & + D_i D_j \sigma^2(r(Q_{\min})) - (D_i f_j + D_j f_i) \text{cov}(r(Q_{\min}), I_0) \\ & \left. + \tilde{\alpha}^j (j+1) D_i \text{cov}(r(Q_{\min}), I_j) + \tilde{\alpha}^i (i+1) D_j \text{cov}(r(Q_{\min}), I_i) \right]. \end{aligned} \quad (\text{A19})$$

Here we have defined

$$\mathcal{N}_m \equiv \frac{1}{2Q_{\min}^{1/2} r(Q_{\min}) / F^2(Q_{\min}) + I_0}, \quad (\text{A20})$$

$$\tilde{\alpha} \equiv \frac{\alpha}{300 \text{ km/s}}, \quad (\text{A21})$$

and

$$D_i \equiv \frac{1}{\mathcal{N}_m} \left[\frac{\partial f_i}{\partial r(Q_{\min})} \right] = \frac{2}{F^2(Q_{\min})} \left(\tilde{\alpha}^i Q_{\min}^{(i+1)/2} - Q_{\min}^{1/2} f_i \right), \quad (\text{A22a})$$

for $i = -1, 1, 2, \dots, n_{\max}$; and

$$D_{n_{\max}+1} = \frac{2}{F^2(Q_{\min})} \left(-Q_{\min}^{1/2} f_{n_{\max}+1} \right). \quad (\text{A22b})$$

References

- [1] P. F. Smith and J. D. Lewin, *Phys. Rep.* **187**, 203 (1990).
- [2] J. D. Lewin and P. F. Smith, *Astropart. Phys.* **6**, 87 (1996).
- [3] G. Jungman, M. Kamionkowski and K. Griest, *Phys. Rep.* **267**, 195 (1996).
- [4] G. Bertone, D. Hooper and J. Silk, *Phys. Rep.* **405**, 279 (2005).
- [5] C. L. Shan and M. Drees, [arXiv:0710.4296 \[hep-ph\]](#) (2007).
- [6] M. Drees and C. L. Shan, *J. Cosmol. Astropart. Phys.* **0806**, 012 (2008).
- [7] M. Drees and C. L. Shan, *J. Cosmol. Astropart. Phys.* **0706**, 011 (2007).
- [8] CDMS Collab., Z. Ahmed *et al.*, [arXiv:0912.3592 \[astro-ph.CO\]](#) (2009).

¹³Since the last f_i defined in Eq. (24b) can be computed from the same basic quantities, i.e., the counting rates at Q_{\min} and the integrals I_0 , it can directly be included in the covariance matrix.

- [9] CRESST Collab., R. F. Lang *et al.*, *Astropart. Phys.* **33**, 60 (2010); CRESST Collab., J. Schmalzer *et al.*, *AIP Conf. Proc.* **1185**, 631 (2009).
- [10] E. Aprile and L. Baudis, for the XENON100 Collab., *PoS IDM2008*, 018 (2008).
- [11] EDELWEISS Collab., A. Broniatowski *et al.*, *Phys. Lett. B* **681**, 305 (2009); EDELWEISS Collab., E. Armengaud *et al.*, *Phys. Lett. B* **687**, 294 (2010).
- [12] CRESST Collab., R. F. Lang *et al.*, *Astropart. Phys.* **32**, 318 (2010).
- [13] N. Bernal, A. Goudelis, Y. Mambrini and C. Munoz, *J. Cosmol. Astropart. Phys.* **0901**, 046 (2009).
- [14] A. M. Green, *J. Cosmol. Astropart. Phys.* **0807**, 005 (2008).
- [15] D. G. Cerdeño and A. M. Green, contribution to “*Particle Dark Matter: Observations, Models and Searches*”, G. Bertone, Cambridge University Press, Chapter 17 (2010), [arXiv:1002.1912 \[astro-ph.CO\]](#).
- [16] K. Freese, J. Frieman and A. Gould, *Phys. Rev. D* **37**, 3388 (1988).
- [17] C. L. Shan, *New J. Phys.* **11**, 105013 (2009).
- [18] J. Engel, *Phys. Lett. B* **264**, 114 (1991).
- [19] <http://pisrv0.pit.physik.uni-tuebingen.de/darkmatter/amidas/>.
- [20] C. L. Shan, *AIP Conf. Proc.* **1200**, 1031 (2010); [arXiv:0910.1971 \[astro-ph.IM\]](#) (2009).
- [21] A. M. Green, *J. Cosmol. Astropart. Phys.* **0708**, 022 (2007).
- [22] P. Sikivie and J. R. Ipser, *Phys. Lett. B* **291**, 288 (1992); P. Sikivie, *Phys. Lett. B* **567**, 1 (2003).
- [23] K. Freese, P. Gondolo, H. J. Newberg and M. Lewis, *Phys. Rev. Lett.* **92**, 111301 (2004).
- [24] A. Natarajan and P. Sikivie, *Phys. Rev. D* **73**, 023510 (2006); *Phys. Rev. D* **76**, 023505 (2007).
- [25] F. S. Ling, P. Sikivie and S. Wick, *Phys. Rev. D* **70**, 123503 (2004).
- [26] L. Baudis, [arXiv:0711.3788 \[astro-ph\]](#) (2007).
- [27] M. Drees and G. Gerbier, contribution to “*The Review of Particle Physics 2008*”, C. Amsler *et al.*, *Phys. Lett. B* **667**, 1 (2008).
- [28] J. Gascon, [arXiv:0906.4232 \[astro-ph.HE\]](#) (2009).
- [29] CoGeNT Collab., C. E. Aalseth *et al.*, [arXiv:1002.4703 \[astro-ph.CO\]](#) (2010).
- [30] W. Seidel, talk given at *WONDER 2010 Workshop*, Laboratory Nazionali del Gran Sasso, Italy, March 22-23, 2010.
- [31] D. Hooper, J. I. Collar, J. Hall and D. McKinsey, [arXiv:1007.1005 \[hep-ph\]](#) (2010).